Biosensors and Bioelectronics 286 (2025) 117611

Contents lists available at ScienceDirect

Biosensors and Bioelectronics

journal homepage: www.elsevier.com/locate/bios

# A CRISPR/Cas12a biosensor for portable and accessible detection of *Salmonella typhimurium* via multi-indicator pH millidisc colorimetry and smartphone imaging platform

Miaolin Duan [a,b,1], Guoqiang Li [a,1], Jingqi Shen [a], Ruitong Dai [b], Xingmin Li [b], Zunying Liu [a], Fei Jia [a,*]

[a] College of Food Science and Engineering, Ocean University of China, Qingdao Shandong, 266100, China
[b] College of Food Science and Nutritional Engineering, China Agricultural University, Beijing, 100083, China

ARTICLE INFO

*Keywords:*
CRISPR/Cas12a
*Salmonella typhimurium*
Colorimetric detection
pH indicator paper
Portable biosensor
Smartphone

ABSTRACT

Conventional colorimetric CRISPR/Cas methods rely on a single chromogenic substrate and bulky and specialized signal detection instrument, which hinder their practical application. Herein, a portable and accessible CRISPR/Cas12a biosensor was for the first time reported to sensitively quantify *Salmonella enterica* serovar *typhimurium* (*S. typhimurium*), utilizing a multi-indicator pH millimeter disc (millidisc) for signal visualization, combined with a smartphone-based imaging platform for signal readout. The pH millidisc, composed of multiple indicators, possessed sensitive pH responsiveness and exhibited diverse color changes. The self-developed RGB mini-program, named DeepFood, was designed for portable smartphone use, featuring user-friendly operation and trend visualization for preliminary result analysis. Based on the RGB signal variation pattern with *S. typhimurium*, a distinct $S_{enh}$ signal type was designed, enhancing the signal-to-noise ratio from 3.38 to 7.11. Compared to the R signal type, the $S_{enh}$ signal type improved detection sensitivity by 36.23-fold (7.26 CFU/mL) in 0.01 M PBS buffer and 15.53-fold ($1.41 \times 10^2$ CFU/mL) in chicken. The proposed biosensor offers significant improvements in detection sensitivity and practical applicability, with potential in food safety and environmental protection.

## 1. Introduction

A promising novel CRISPR/Cas-based rapid detection method has emerged (Li et al., 2022). The Cas endonucleases (e.g., Cas9, Cas12a, Cas13) form binary complexes with guide RNA to achieve rapid and highly specific recognition of nucleic acid from pathogenic bacteria (Li et al., 2021). Upon target binding, these nucleases undergo conformational rearrangements that expose the RuvC domain(Swarts and Jinek, 2019), activating their nucleic acid cleavage capabilities and triggering signal generation. To expand the applicability of CRISPR/Cas-based methods in field testing and diverse scenarios, the development of portable and user-friendly instrument is essential (Qiu et al., 2022). Detection instruments are broadly categorized into those for sample pre-treatment and those for signal readout. Sample pre-treatment, involves nucleic acid extraction and amplification, traditionally performed with standard laboratory instruments such as water baths, centrifuges, and PCR machines. While these devices are reliable and versatile, they are not the primary focus for enhancing detection performance. Alternative methods, such as boiling for DNA extraction and the use of recombinase polymerase amplification (RPA) or recombinase-aided amplification (RAA) kits (Zhao et al., 2024), offer significant time savings and reduced reliance on complex instruments. In contrast, signal detection instrument significantly impacts the sensitivity and accuracy of both qualitative and quantitative outcomes, thereby meriting careful consideration. Specialized instruments like UV-visible spectrophotometers (Zhang et al., 2021), fluorescence spectrometers (Chen et al., 2020), electrochemical workstations (Liu et al., 2022), and Raman spectrometers (Choi et al., 2021) deliver excellent performance but are often bulky, expensive, and operationally complex, limiting their suitability for on-site applications (Shi et al., 2024). Significant efforts have been made to develop portable signal readout instruments. For example, Tanifuji et al. utilized a portable glucometer to

* Corresponding author.
*E-mail address:* feijia@ouc.edu.cn (F. Jia).
[1] These authors contributed equally to this work.

https://doi.org/10.1016/j.bios.2025.117611
Received 9 January 2025; Received in revised form 13 April 2025; Accepted 19 May 2025
Available online 20 May 2025
0956-5663/© 2025 Elsevier B.V. All rights are reserved, including those for text and data mining, AI training, and similar technologies.

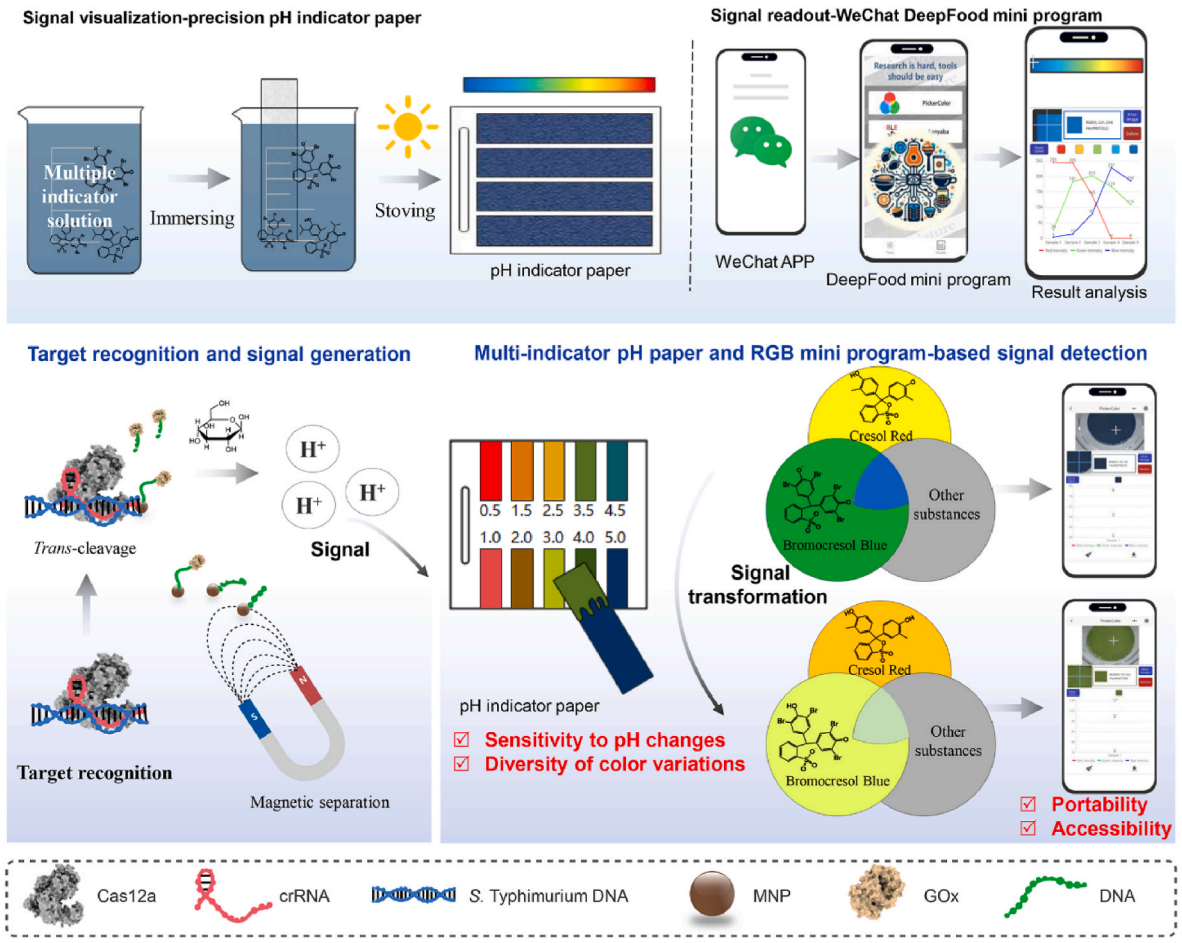



**Fig. 1.** Schematic illustration of the proposed biosensor system, which integrated target recognition, signal generation, and signal detection. The signal detection system comprised a multi-indicator pH millidisc for visual signal output and the DeepFood mini-program for digital signal detection and analysis.

detect glucose signals induced by human papilloma virus (Tanifuji et al., 2024), while Zhao et al. employed a simple pH meter to monitor pH signal changes with and without aflatoxin $B_1$ (Zhao et al., 2018). Similarly, Uygun et al. and Zeng et al. used miniaturized electrochemical (Uygun et al., 2020) and pressure-sensitive chips (Zeng et al., 2021) for signal readout. Although these approaches rely on compact and portable devices, such instruments remain specialized and are not widely accessible to the general public, limiting their widespread availability.

The pH-responsive colorimetric detection method utilizes target-induced pH shifts to trigger color transitions in chromogenic reagents, providing intuitive visual signals suitable for on-site detection (Gong et al., 2021). For example, Ki et al. developed a urease-based signal probe, in which urease catalyzes the alkalization of the solution, causing the indicator phenol red to transition from yellow to red (Ki et al., 2022). Xiong et al., (2017) and Pei et al., (2018a) employed the acid-base indicator bromocresol purple dye to visualize changes in the solution pH. These methods predominantly rely on a single chromogenic substance to indicate pH changes triggered by the target. They suffer from low pH response sensitivity, a limited detection range, and a lack of diverse color transitions, which restrict its utility in semi-quantitative and high-sensitivity detection applications. Researchers have utilized the etching of gold nanoflowers and nanorods to modulate localized surface plasmon resonance (LSPR) by altering their shape, size, and surface characteristics, thereby generating diverse color variations. For instance, Pei et al. demonstrated that target-induced etching of gold nanoflowers could produce even more pronounced color changes (Pei et al., 2018b). Besides, Huang et al., (2020) and Xiong et al., (2018) achieved vibrant and dynamic color shifts by employing target-triggered etching of gold nanorods. This approach enables diverse color variations, facilitating effective semi-quantitative detection with the naked-eye. However, the reliance on nanomaterials renders the system susceptible to environmental factors and poses challenges for long-term storage.

To address these challenges, a signal detection system integrated with multi-indicator pH millimeter disc (millidisc) and smartphone RGB mini-program was proposed, aiming to overcome the limitations of conventional single chromogenic systems and bulky instruments in CRISPR/Cas-based pathogen detection. The multi-indicator pH millidisc, composed of cresol red, bromocresol blue, and bromothymol blue, was used for signal visualization. It exhibited a sensitive pH response and a rich variety of color changes, which contributed to enhancing the detection sensitivity. The smartphone-based self-developed DeepFood mini-program was used for signal readout. It was multi-platform compatible, useable on both computers and smartphones for greater flexibility. Built on WeChat, a widely used social app in China, it operated efficiently within the platform. Additionally, its trend analysis feature enabled intuitive visualization of result variations. To the best of our knowledge, this is the first attempt to develop and integrate a multi-indicator pH millidisc with a smartphone-based RGB readout system for CRISPR/Cas-based pathogen detection. In a word, it could expand CRISPR/Cas diagnostics to more accessible, decentralized, and resource-limited applications.

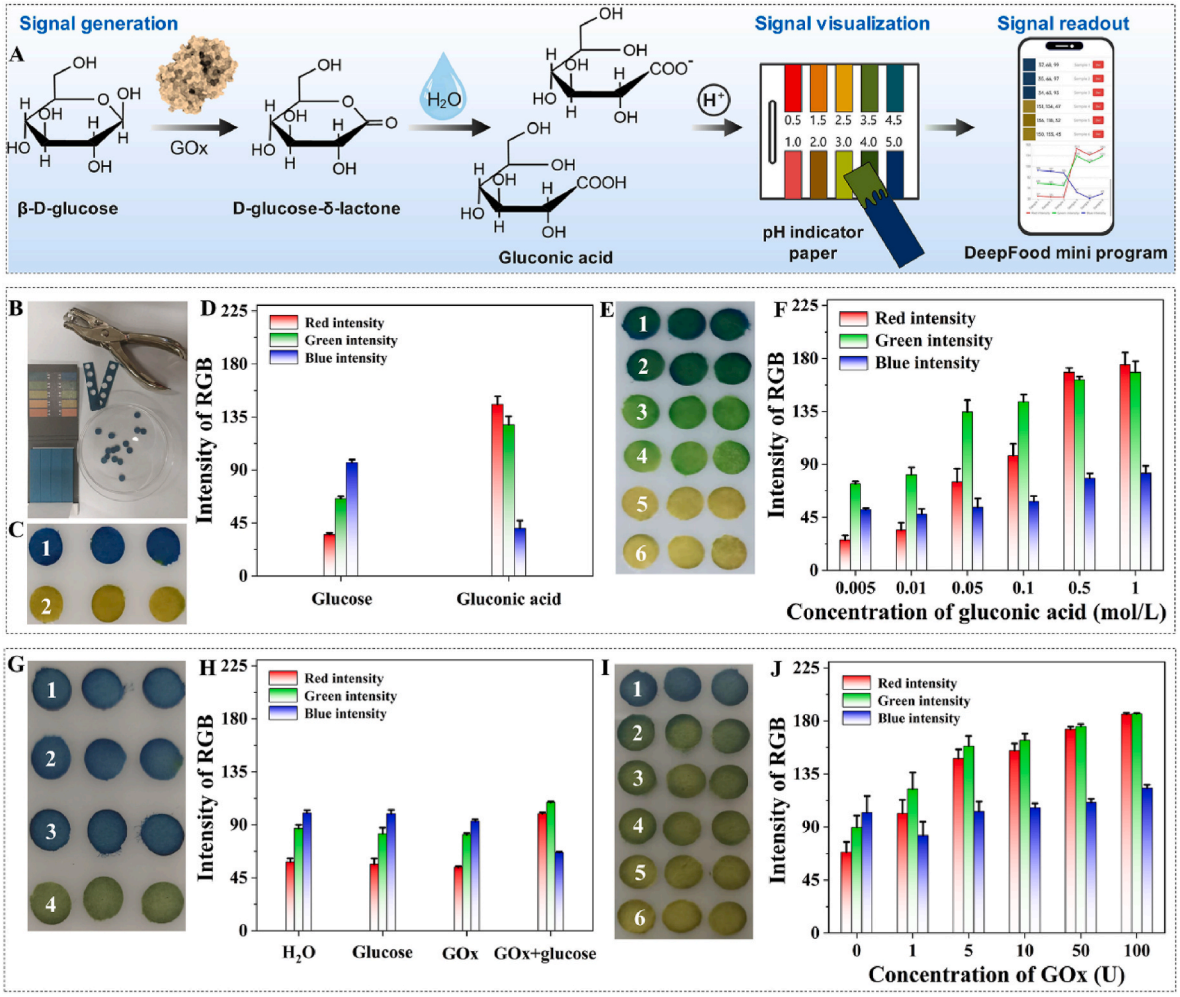



**Fig. 2.** (A) Schematic illustration of the signal system. (B) The preparation for pH millidiscs. Verification of pH differentiation between glucose and gluconic acid through (C) naked-eye (1: glucose, 2: gluconic acid) and (D) DeepFood mini-program. Analysis of pH responses to different gluconic acid concentrations via (E) naked-eye (1-6: 0.005-1 mol/L gluconic acid) and (F) DeepFood mini-program. Verification of pH variation induced by GOx through (G) naked-eye (1: $H_2O$, 2: glucose, 3: GOx, 4: GOx + glucose) and (H) DeepFood mini-program. Analysis of pH responses to different GOx concentrations via (I) naked-eye (1-6: 0-100 U GOx) and (J) DeepFood mini-program.

## 2. Experimental sections

### 2.1. Detection procedure of the proposed biosensor

Before detection, the samples were pretreated with DNA extraction and amplification steps for further analysis. The detailed procedures for bacteria culture and pretreatment are provided in Supplementary Material 2.1 and 2.2. The detection procedure was as follows: firstly, 10 μL of enzyme-free sterile water, 10 μL of 10 × NEBuffer, 10 μL of 1 μM Cas12a (0.01 nmol), and 10 μL of 1 μM crRNA (0.01 nmol) were mixed and incubated at 25 °C for 10 min (The oligonucleotide sequences are presented in Table S1). Then, 20 μL of the above pretreated sample was added and incubated at 37 °C for 10 min. Next, 40 μL of the nanoreporter (Supplementary Material 2.5) was added and incubated at 37 °C for 1 h. The nanoreporter was prepared by mixing of latex nanoparticle (LNP) labeled with linker DNA and glucose oxidase (LNP-DNA-GOx conjugate) and magnetic nanoparticle labeled with SA (MNP-SA conjugate), followed by magnetic separation and resuspension in PBS. Following this, magnetic separation was performed. Then, 100 μL of 1 M β-D-glucose solution (100 μmol) was added and incubated at 37 °C for 90 min. Subsequently, 5 μL of the above solution was added dropwise to the circular pH millidisc prepared with a punch. A smartphone-based DeepFood mini-program was used to photograph and analyze the color change of pH millidisc, converting the color into numerical values. The detailed experimental methods for the evaluation of sensitivity and specificity are described in the Supplementary Material 2.6 and 2.7. Line fitting analysis was conducted using Origin software to construct the calibration curve.

### 2.2. Application evaluation

The feasibility of the proposed biosensor was evaluated using chicken samples. Firstly, chicken sample was minced under sterile conditions. Then, 25 g of the minced chicken and 225 mL of sterile 0.01 M PBS buffer were added to a sterile sampling bag for homogenization. Subsequently, *Salmonella enterica* serovar *typhimurium* (*S. typhimurium*) was gradually spiked into the supernatant after homogenization. The detection procedures followed the proposed protocol above.

## 3. Results and discussion

### 3.1. Working principle of the proposed biosensor

This study aims to utilize the nucleic acid recognition and cleavage capabilities of Cas12a to establish a correlation between the presence of *S. typhimurium* and pH signal variations. Based on this principle, the

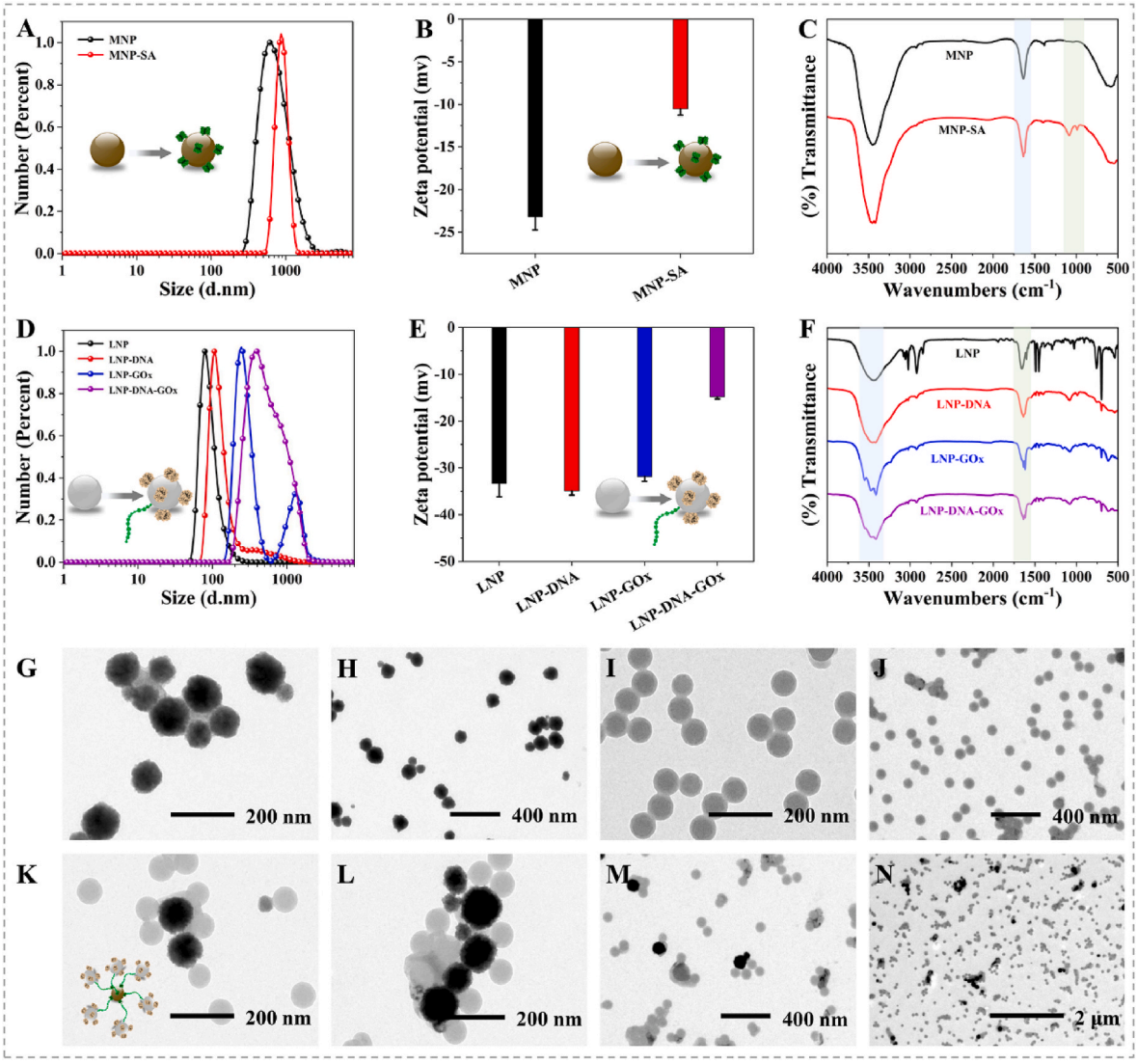



**Fig. 3.** Particle size (A), Zeta potential (B), and infrared spectra (C) of MNPs before and after SA labeling. Particle size (D), Zeta potential (E), and infrared spectra (F) of LNP before and after DNA and GOx conjugation. (G-H) TEM images of MNP-SA at different magnifications. (I-J) TEM images of LNP-DNA-GOx at different magnifications. (K-N) TEM images of the assembled nanoreporter at different magnifications.

multi-indicator pH millidisc and self-developed DeepFood mini program-mediated signal detection system was developed to enable portable detection of *S. typhimurium* (Fig. 1). The study consists of three main components: target recognition, signal generation, and portable signal detection.

For target recognition, when *S. typhimurium* DNA is present, it was specifically recognized by the crRNA within the Cas12a-crRNA duplex through base-pairing, forming a Cas12a-crRNA-*S. typhimurium* DNA ternary complex. This recognition triggered a conformational change in the Cas12a enzyme, exposing its RuvC domain and activating its cleavage function(Swarts and Jinek, 2019), enabling indiscriminate cleavage of nearby single-stranded DNA; For signal generation, the activated Cas12a cleaved the linker DNA in the nanoreporter, which was designed with MNP at one end and GOx at the other end. This cleavage disconnected the linkage between MNP and GOx, leading to the release of GOx. Following magnetic separation, the freed GOx catalyzed the conversion of β-D-glucose into gluconic acid, which ionized to release $H^+$, generating the pH signal; The final step was signal detection, which consisted of multi-indicator pH millidisc-mediated signal visualization and a self-developed DeepFood mini program-based signal readout. The pH millidisc, composed with multi-indicator including cresol red, bromocresol blue, bromothymol blue, was sensitive to pH changes and showed diversity of color variations. As the $H^+$ concentration increased, the color of the pH millidisc gradually shifted from blue to yellow, providing a clear visual representation of the signal. For signal readout, the DeepFood mini-program was used for RGB signal measurement. With the color change, the red (R) and green (G) values increased, while the blue (B) value decreased, enabling digital interpretation of the pH-based signal.

### 3.2. Feasibility validation of signal output system

The schematic diagram of the signal output system was illustrated in Fig. 2A, including GOx catalyzing β-D-glucose to gluconic acid, pH millidisc visualizing the pH of solution, and DeepFood mini-program measuring RGB value. To achieve uniform signals, pH millidisc was perforated using a puncher with a diameter of 6 mm (Fig. 2B). Initially, pH millidisc was employed to measure glucose (1 M) and gluconic acid solution (1 M), followed by photography and signal processing (Supplementary Material 2.4). As shown in Fig. 2C, the results observed with naked-eye displayed glucose and gluconic acid appearing as blue and yellow colors respectively on the pH millidiscs. By referencing the

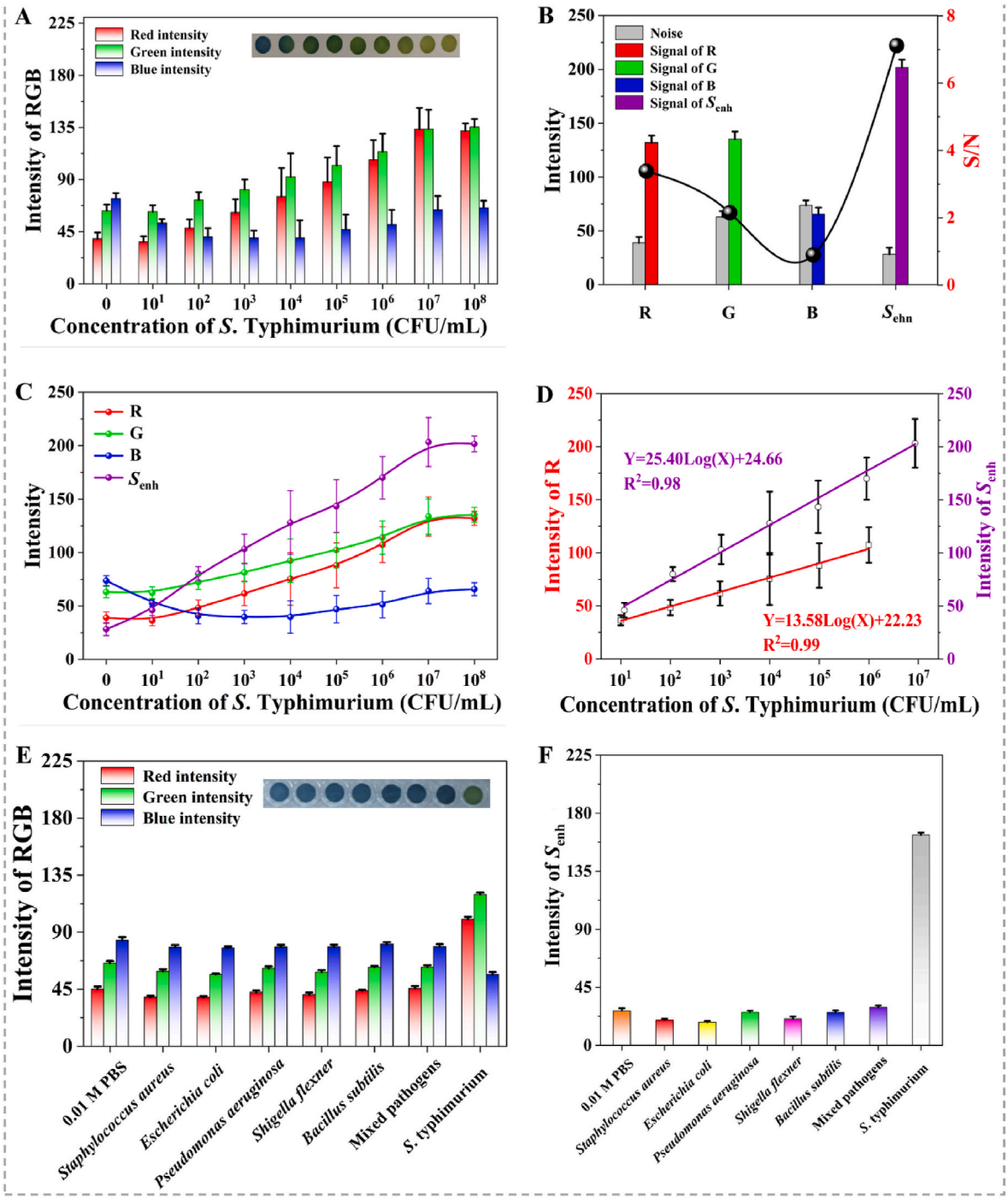



**Fig. 4.** (A) Detection of varying concentrations of *S. typhimurium* (0-$10^8$ CFU/mL) utilizing the proposed biosensor. (B) The S/N of different signal output types. (C) Calibration curve illustrating the performance of the proposed biosensor with different signal output types. (D) Quantitative calibration curve of the proposed biosensor utilizing R and $S_{enh}$ signal output types. Specificity evaluation for *S. typhimurium* ($10^6$ CFU/mL) using this biosensor with (E) RGB and (F) $S_{enh}$ signal output type.

pH millidisc color chart, the pH levels of glucose and gluconic acid were estimated to be approximately 5 and 2, respectively. Subsequently, the results were analyzed using the DeepFood mini-program. The results were illustrated in Fig. 2D, where the RGB values of glucose were 35.33 ± 1.25, 65.67 ± 2.05, and 96.33 ± 2.49, respectively. The RGB values of gluconic acid were 145.67 ± 6.85, 128.33 ± 7.32, and 40.67 ± 6.34, respectively. The interface and part of the code of the DeepFood mini-program were shown in Fig. S1. The detailed usage steps of DeepFood were listed in Fig. S2 and S3.

To validate the dose-response relationship between gluconic acid concentration and pH, pH millidiscs were utilized to measure gluconic acid solutions with varying concentrations (0.005-1 mol/L). The results observed by naked-eye indicated a gradual color change of the pH millidiscs from green to yellow with increasing concentrations of gluconic acid (Fig. 2E). The results outputted by the DeepFood mini-program were displayed in Fig. 2F and Fig. S4, where an upward trend in RGB values was observed with increasing concentrations. Specifically, the R value exhibited the most significant signal change, increasing from 24.31 ± 3.74 to 177.23 ± 10.40 with rising concentrations. To evaluate the reliability of the smartphone-based DeepFood

RGB mini-program, a comparative analysis was conducted with another widely used color analysis software, ColorGrab. As shown in Fig. S5, the RGB readings obtained from both programs were largely consistent, indicating that the DeepFood RGB mini-program exhibited good comparability with ColorGrab in terms of signal processing.

To verify that pH variation can be induced by GOx, different experimental groups were set up ($H_2O$, glucose, GOx, and GOx + glucose). As observed with the naked eye in Fig. 2G, in the presence of both GOx and glucose, the pH millidisc turned green, indicating a pH of approximately 3 according to the pH chart. In contrast, the other groups showed blue color, correlating to a pH of about 5. The results outputted by the DeepFood mini-program indicated that in the presence of both GOx and glucose, compared to the other three control groups, the R value increased from 54.00 ± 0.82 to 99.33 ± 1.25, the G value from 81.67 ± 1.25 to 109 ± 0.82, and the B value decreased from 93.00 ± 1.63 to 66.33 ± 0.95 (Fig. 2H). To further validate the dose-response relationship between the concentration of GOx and pH, pH millidiscs were used to measure solutions catalyzed by different concentration of GOx. The results observed by naked-eye showed a gradual color change from blue to yellow with increasing GOx concentrations (0-100 U) (Fig. 2I). The results outputted by the DeepFood mini-program demonstrated that the R value gradually increased from 68.67 ± 8.73 to 185.67 ± 1.25, the G value from 89.67 ± 10.14 to 186 ± 0.82, while the B value showed minimal change, remaining within the range of 83.00 ± 11.52 to 123 ± 2.94 (Fig. 2J). In summary, the GOx was able to induce pH variation indicating the feasibility of signal output system.

### 3.3. Characterization of nanoreporter

As the core component of the signal generation system, the nanoreporter consisted of MNP-SA conjugate and LNP-DNA-GOx conjugate. To verify the successful modification of functional components onto the nanoparticle carriers, the hydration particle size, Zeta potential, and infrared spectra of the MNP and LNP were measured before and after labeling. The results for the MNP indicated that after SA labeling, the particle size increased from 615 nm to 825 nm (Fig. 3A). The absolute value of the Zeta potential decreased from 23.20 ± 1.56 to 10.55 ± 0.74 (Fig. 3B). The infrared spectroscopy of the MNPs was illustrated in Fig. 3C. The MNP before labeling exhibited a C=O stretching vibration peak at 1638 $cm^{-1}$, likely due to the presence of carboxyl groups on the surface of the MNP. After labeling with SA, a new peak appeared at 1621 $cm^{-1}$ and a C-N stretching vibration peak were observed at 1085 $cm^{-1}$, indicating the successful coupling of SA to the MNPs. The experimental results of LNP (Fig. 3D) shown that the particle size was 78.8 nm before labeling. After labeling with linker DNA, GOx, and both DNA and GOx, the LNP increased to 106 nm, 255 nm, and 396 nm, respectively. Notably, the LNP labeled solely with GOx showed two peaks of different intensities, with the higher intensity peak corresponding to a particle size of 225 nm, and the lower intensity peak corresponding to a particle size of 1280 nm. The possible reason was that a small amount of cross-linking occurred during the coupling process, likely due to multiple amino groups on GOx condensing with carboxyl groups on different LNP. However, this phenomenon disappeared when both linker DNA and GOx were labeled, indicating that the coupling of linker DNA weakened the cross-linking of LNP during the labeling process. The Zeta potential results (Fig. 3E) showed a gradual decrease in the absolute value after labeling. Infrared spectroscopy results shown that, LNP-DNA, LNP-GOx, and LNP-DNA-GOx exhibited stronger C=O stretching vibration peaks at 1659.22 $cm^{-1}$ (Fig. 3F), compared to LNP. It was likely due to the abundance of C=O groups in DNA and GOx. Additionally, LNP-DNA and LNP-DNA-GOx showed characteristic phosphate stretching vibration peaks at 988.82 $cm^{-1}$, which were not present in the LNP and LNP-GOx. Additionally, an N-H stretching vibration peak is observed at 3474 $cm^{-1}$. These above results indicated that linker DNA and GOx were successfully labeled onto the LNPs.

Transmission electron microscopy (TEM) was subsequently used to observe the size and distribution of nanoreporter. As shown in Fig. 3G and 3H, the MNP-SA was uniformly dispersed with a spherical shape with a particle size of about 100.93 ± 23.43 nm (Fig. 3I and Fig. S7A). Similarly, the LNP-DNA-GOx also exhibited good dispersibility with a particle size of about 81.27 ± 2.09 nm (Fig. 3J and Fig. S7B). After mixing and incubating the two types of conjugates, TEM was conducted. Theoretically, the SA on the MNP-SA conjugate and the biotin carried by one end of the linker DNA on the LNP-DNA-GOx conjugate bind through non-covalent interactions, forming the nanoreporter. As shown in Fig. 3K-3N, under different magnifications, the MNP-SA conjugate was observed to bind with the LNP-DNA-GOx conjugate, indicating the successful preparation of nanoreporter. The resulting signal nanoreporter, MNP-DNA-LNP-GOx, utilized LNP as carriers to enhance GOx loading capacity. This design facilitated an increased release of GOx per single cleavage event mediated by Cas12a, thereby contributing to the analytical sensitivity of the method.

### 3.4. Performance evaluation of the proposed biosensor

To evaluate the feasibility of the constructed method, *S. typhimurium* was diluted in 0.01 M PBS buffer for detection. The detection process takes approximately 3 h from the sample pre-treatment to the final result readout. The results observed by naked-eye indicated that with increasing concentrations of *S. typhimurium*, the color of the pH millidiscs gradually changed from blue to yellow (Fig. 4A). According to the comparison with the pH chart, the pH decreased from 5 to 3. Notably, as the pH gradually decreased, the color distribution of the circular pH millidisc became increasingly uneven. Within a certain concentration range, some of the multi-indicator components undergo color changes due to protonation, while others retain their original color. As a result, the pH millidisc contains multiple-colored indicators, creating a diverse and vibrant color presentation. Furthermore, the evaporation rate of differently colored indicators was higher at the edges, causing liquid to flow from the center toward the edge. This led to an increased concentration of the indicator at the edges, resulting in the coffee ring effect (Yang et al., 2022). To standardize the data acquisition region, an auxiliary reading ring (Fig. S2) was used to define a circular area with a 3 mm diameter at the center of the pH millidisc as the designated detection area, ensuring data stability and comparability. The cut-off value for distinguishing negative and positive results was determined as the mean of negative samples plus three times the standard deviation. Results showed that all ten negative samples were below the cut-off, indicating no false positives (Fig. S17).

As shown in Fig. 4A, the R and G signals increased with the concentration, while the B signal generally decreased with the increasing concentration. To obtain optimal concentration-signal variation, different signal-to-noise ratio (S/N) of RGB signal types were compared. The results showed that the S/N of the R, G, and B signal types were 3.38, 2.15, and 0.89, respectively. The R signal type had the highest S/N. As shown in Fig. 4A, the concentration-signal relationship exhibited the following trend: the R and G values increased with the concentration of *S. typhimurium*, while the B value showed a general decreasing trend. To achieve more pronounced concentration-signal variations, an enhanced signal type ($S_{enh}$) was designed to enhance signal changes, enabling high sensitivity detection.

$$S_{enh}=R + G-B$$

Compared to R signal type, the negative signal of $S_{enh}$ signal type decreased from 39.00 to 28.33, and the positive signal increased from 132.00 to 201.67. The S/N was improved to 7.11. This demonstrated that the $S_{enh}$ signal type amplified signal variation.

To evaluate the feasibility of $S_{enh}$ signal type, the $S_{enh}$ signals of different concentrations of *S. typhimurium* were observed. As depicted in Fig. 4C, the $S_{enh}$ signal increased with the concentration of *S. typhimurium*, showing an appropriate trend. As shown in Fig. 4D, for

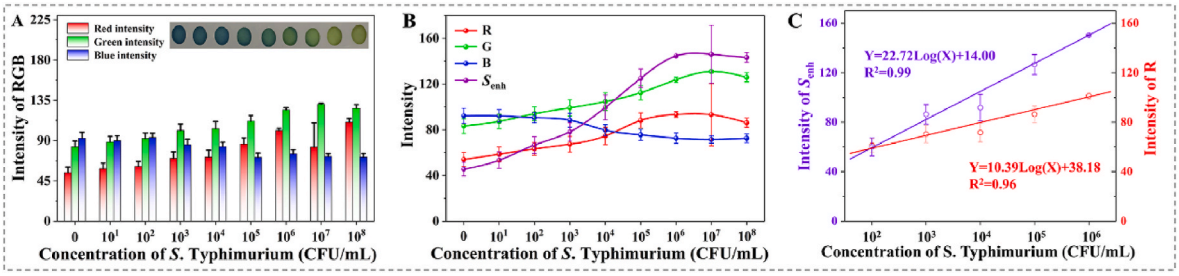



**Fig. 5.** (A) Detection of varying concentrations of *S. typhimurium*-spiked chicken samples (0-$10^8$ CFU/mL) employing the proposed biosensor. (B) Calibration curve of *S. typhimurium*-spiked chicken samples with different signal output types. (C) Quantitative calibration curve of *S. typhimurium*-spiked chicken samples utilizing R and $S_{enh}$ signal types.

the R signal type, the linear equation was Y=13.58Log(X) + 22.23 with an $R^2$ of 0.99, and the linear range was $10^1$-$10^6$ CFU/mL. For the $S_{enh}$ signal type, the linear equation was Y=25.40Log(X) + 24.66 with an $R^2$ of 0.98, and the linear range was $10^1$-$10^7$ CFU/mL. The limits of detection (LOD) for the two signal types were calculated to be 2.63 × $10^2$ CFU/mL and 7.26 CFU/mL, respectively. The $S_{enh}$ signal type enhanced the sensitivity by 36.23-fold. This demonstrated that the proposed biosensor had high sensitivity. The versatility of this method was determined by the crRNA. After replacing it with a *Staphylococcus aureus*-specific crRNA (Zhou et al., 2022), the method achieved successful detection of *Staphylococcus aureus* with a LOD of 79 CFU/mL (Fig. S18).

To evaluate the specificity of the constructed biosensor, five common foodborne pathogens were detected both individually and in a mixed sample. Details of the bacterial strains are provided in Table S2. Using 0.01 M PBS buffer solution as the negative control, the measured RGB values were 45.125 ± 1.96, 65.5 ± 1.66, and 83.75 ± 2.28. Subsequently, five non- *S. typhimurium* pathogens were tested both individually and in a mixed sample. The results showed that, when tested individually, the RGB values for the five non- *S. typhimurium* pathogens ranged from 38.625 ± 0.86 to 43.75 ± 0.83, 56.75 ± 0.66 to 62.38 ± 0.86, and 77.5 ± 1.32 to 80.63 ± 1.49, respectively (Fig. 4E). In the mixed sample, the five pathogens yielded RGB values of 45.75 ± 1.79, 62.5 ± 1.41, and 78.75 ± 1.79. No substantial differences were observed between the negative control and the five non- *S. typhimurium* pathogens. In contrast, *S. typhimurium* displayed marked changes in RGB values, with R and G increasing to 100.25 ± 1.85 and 119.75 ± 1.64, respectively, and B decreasing to 56.875 ± 1.69. The results for the $S_{enh}$ signal type were similar (Fig. 4F) but with more pronounced signal variation. This demonstrated that the proposed biosensor had good specificity.

To assess the applicability of the constructed biosensor, *S. typhimurium*-spiked chicken samples were detected. As shown in Fig. 5A and 5B, with increasing concentrations of *S. typhimurium*, the R, G, and $S_{enh}$ values showed an upward trend, while B values showed a downward trend. Subsequently, the signals were linearly fitted with the *S. typhimurium* concentration to calculate and evaluate the sensitivity of the biosensor. As shown in Fig. 5C, for the R signal type, the linear equation was Y=10.39Log(X) + 38.18 with an $R^2$ of 0.96, and the linear range was $10^2$-$10^6$ CFU/mL. For the $S_{enh}$ signal type, the linear equation was Y=22.72Log(X) + 14.00 with an $R^2$ of 0.99, and the linear range was $10^2$-$10^6$ CFU/mL. The LOD for the two signal types were calculated to be 2.19 × $10^3$ CFU/mL and 1.41 × $10^2$ CFU/mL, respectively. The $S_{enh}$ signal type increased the sensitivity by 15.53-fold. Notably, a weighted linear regression was applied in this study, where each data point was assigned a weight equal to the inverse square of its measurement error ($w_i=1/e_i^2$). Compared to unweighted regression, the weighted approach emphasizes data points with smaller errors and higher quality, allowing the fitted curve to more closely align with those reliable points. For comparison, unweighted linear regression-assuming equal weights for all data points-was also performed, in which the fitted curve attempts to minimize the average distance from all data regardless of data quality. The resulting equations were as follows: for the R signal type, Y=9.60Log(X) + 39.80 with an $R^2$ of 0.91; and for the $S_{enh}$ signal type, Y=22.10Log(X) + 14.60 with an $R^2$ of 0.95. The spiked recovery results showed that the CV value (7.34 %-18.16 %) was within an acceptable range (Table S3). This demonstrated that the proposed biosensor had potential applicability.

## 4. Conclusion

In summary, a CRISPR/Cas12a-based biosensor for portable and accessible detection of *S. typhimurium* was developed, utilizing multi-indicator pH millidisc colorimetry combined with smartphone imaging system. This approach provided a user-friendly, on-site signal detection platform, reducing the reliance on sophisticated laboratory instruments. Based on the RGB signal variation pattern with *S. typhimurium* DNA, an $S_{enh}$ signal type was designed, improving the S/N ratio from 3.38 to 7.11. The sensitivity of the R and $S_{enh}$ signal type in buffer solution were 2.63 × $10^2$ CFU/mL and 7.26 CFU/mL, respectively, representing a 36.23-fold improvement in sensitivity with the designed type. In chicken samples, the sensitivities of the R and $S_{enh}$ signal types were 2.19 × $10^3$ CFU/mL and 1.41 × $10^2$ CFU/mL, respectively, demonstrating a 15.53-fold improvement. Despite the promising results, certain limitations remain. Detection accuracy may be affected by the environmental factors, such as lighting variations during smartphone imaging. Additionally, sample preparation requires further simplification to improve practicality. To improve accessibility for non-expert users, a deep learning model can be integrated to enable direct result output from captured images, eliminating manual RGB extraction and analysis. Future efforts will focus on stabilizing the imaging environment, streamlining sample preparation, and incorporating AI-based models to achieve more user-friendly and intelligent detection, thereby broadening the platform's applicability across diverse diagnostic conditions.

## CRediT authorship contribution statement

**Miaolin Duan:** Writing – original draft, Validation, Methodology, Investigation, Formal analysis, Data curation, Conceptualization. **Guoqiang Li:** Writing – original draft, Validation, Methodology, Investigation, Formal analysis, Data curation, Conceptualization. **Jingqi Shen:** Writing – original draft, Formal analysis, Conceptualization. **Ruitong Dai:** Writing – review & editing, Supervision, Project administration, Conceptualization. **Xingmin Li:** Writing – review & editing, Supervision, Project administration, Conceptualization. **Zunying Liu:** Writing – review & editing, Supervision. **Fei Jia:** Writing – review & editing, Supervision, Project administration, Methodology, Investigation, Funding acquisition, Formal analysis, Data curation, Conceptualization.

## Declaration of competing interest

The authors declare that they have no known competing financial

interests or personal relationships that could have appeared to influence the work reported in this paper.

## Acknowledgment

This study was funded by the Taishan Scholar Foundation of Shandong Province (tsqn202408082).

## Appendix A. Supplementary data

Supplementary data to this article can be found online at https://doi.org/10.1016/j.bios.2025.117611.

## Data availability

Data will be made available on request.

## References

Chen, Y., Shi, Y., Chen, Y., Yang, Z., Wu, H., Zhou, Z., Li, J., Ping, J., He, L., Shen, H., Chen, Z., Wu, J., Yu, Y., 2020. Biosens. Bioelectron. 169, 112642.
Choi, J., Shin, M., Yang, L., Conley, B., Yoon, J., Lee, S., Lee, K., Choi, J., 2021. ACS Nano 15 (8), 13475–13485.
Gong, S., Zhang, S., Wang, X., Li, J., Pan, W., Li, N., Tang, B., 2021. Anal. Chem. 93 (45), 15216–15223.
Huang, D., Qian, J., Shi, Z., Zhao, J., Fang, M., Xu, Z., 2020. ACS Synth. Biol. 9 (11), 3114–3123.
Ki, J., Na, H.K., Yoon, S.W., Le, V.P., Lee, T.G., Lim, E.K., 2022. ACS Sens. 7 (12), 3940–3946.
Li, F., Ye, Q., Chen, M., Xiang, X., Zhang, J., Pang, R., Xue, L., Wang, J., Gu, Q., Lei, T., XianhuWei, Ding, Y., Wu, Q., 2021. Anal. Chim. Acta 1151, 338248.
Li, Y., Man, S., Ye, S., Liu, G., Ma, L., 2022. Compr Rev Food Sci F 21 (4), 3770–3798.
Liu, N., Liu, R., Zhang, J., 2022. Bioelectrochemistry 146, 108105.
Pei, K., Xiong, Y., Li, X., Jiang, H., Xiong, Y., 2018a. Anal. Methods 10 (1), 30–36.
Pei, K., Xiong, Y., Xu, B., Wu, K., Li, X., Jiang, H., Xiong, Y., 2018b. Sensor Actuat B-Chem 262, 102–109.
Qiu, M., Zhang, J., Pang, L., Zhang, Y., Zhao, Q., Jiang, Y., Yang, X., Man, C., 2022. Trends Food Sci Tech 129, 364–387.
Shi, R., Zhong, L., Liu, G., Mak, W.C., 2024. Trac-Trend Anal Chem, 177.
Swarts, D.C., Jinek, M., 2019. Mol. Cell 73, 589–600.
Tanifuji, Y., Tong, G., Hiruta, Y., Citterio, D., 2024. Analyst 149 (19), 4932–4939.
Uygun, Z.O., Yeniay, L., Sağı, F.G., 2020. Anal. Chim. Acta 1121, 35–41.
Xiong, Y., Pei, K., Wu, Y., Duan, H., Lai, W., Xiong, Y., 2018. Sensor Actuat B-Chem 267, 320–327.
Xiong, Y., Pei, K., Wu, Y., Xiong, Y., 2017. Food Control 78, 317–323.
Yang, M., Chen, D., Hu, J., Zheng, X., Lin, Z.-J., Zhu, H., 2022. Trac-Trend Anal Chem, vol. 157.
Zeng, R., Wang, W., Chen, M., Wan, Q., Wang, C., Knopp, D., Tang, D., 2021. Nano Energy 82 (105711).
Zhang, W.S., Pan, J., Li, F., Zhu, M., Xu, M., Zhu, H., Yu, Y., Su, G., 2021. Anal. Chem. 93 (8), 4126–4133.
Zhao, M., Wang, P., Guo, Y., Wang, L., Luo, F., Qiu, B., Guo, L., Su, X., Lin, Z., Chen, G., 2018. Talanta 176, 34–39.
Zhao, Y., Yu, Q., Duan, M., Zhang, Q., Li, Z., Zhang, Y., Liu, Y., Wang, H., Li, X., Dai, R., Jia, F., 2024. J. Agric. Food Chem. 72 (46), 25987–25996.
Zhou, B., Ye, Q., Li, F., Xiang, X., Shang, Y., Wang, C., Shao, Y., Xue, L., Zhang, J., Wang, J., Ding, Y., Chen, M., Wu, Q., 2022. Sensor. Actuator. B Chem. 351.